High-resolution spectroscopic study of hot electron induced copper M-shell charge states emission from laser produced plasmas

F.P. Condamine, E. Filippov, P. Angelo, S.A. Pikuz, O. Renner, F.B. Rosmej

Version of Record: https://www.sciencedirect.com/science/article/pii/S1574181819300242
Manuscript_5199ee711da444e94fc8f4a31277d828

High-resolution spectroscopic study of hot electron induced copper M-shell charge states emission from laser produced plasmas

F.P. Condamine[1,2,3,*], E. Filippov[4,5], P. Angelo[2,3], S.A. Pikuz[4,5], O. Renner[1,6], F.B. Rosmej[2,3,5]

[1]Institute of Physics of Czech Academy of Sciences, ELI Beamlines, 18221 Prague, Czech Republic
[2]Sorbonne University, Faculty of Science and Engineering, UMR7605, case 128, 4 place Jussieu, 75252 Paris Cedex 05, France
[3]LULI, Ecole Polytechnique, CNRS, CEA, Route de Saclay, 91128 Palaiseau, France
[4]Joint Institute for High Temperatures of Russian Academy of Science, 115409 Moscow, Russia
[5]National Research Nuclear University MEPhI, Plasma Physics Department, 115409 Moscow, Russia
[6]Institute of Plasma Physics of Czech Academy of Sciences, 18200 Prague, Czech Republic

***florian.condamine@eli-beams.eu**

Theoretically predicted red shifts of the Cu Kα emission from partly populated M-shell ionic states have been studied in experiments performed at the LULI2000 kJ-ns laser facility. The X-ray spectra were recorded by using three spherically bent crystal spectrometers providing a very high spatial ($\delta x \approx 7\ \mu m$) and spectral ($\lambda/\Delta\lambda \approx 3100$) resolution. The spatially resolved profiles of Kα lines are characterized by red shifts due to a strong overlap of X-ray lines emitted from low charge states at the initial phase of the laser-matter interaction.
Detailed theoretical interpretation of the spectra based on multi-configuration Hartree-Fock simulations provided the population factors of each charge state of 3s and 3p subshells. The advanced diagnostic presented here provides a vehicle for studying the hot and/or dense plasmas in transient environments and gives important information about hot electrons induced X-ray line emission.

Keywords:
Atomic physics
Hot dense plasmas
Hot electrons
X-ray emission spectroscopy

1. Introduction

Laser driven plasmas represent unique systems for investigation of diverse phenomena occurring in extremely hot and dense environments such as stars or planet interiors. Among numerous techniques used for studies of these plasmas, the X-ray emission spectroscopy (XES) is very effective and provides unique possibilities for their characterization[1-3].
When a high-power laser heats the plasma, ions start to emit X-rays. The type of lines emitted as well as their intensity give important information about the plasma itself. The wavelengths of bound-bound transitions characterize the emitting elements and their ionization state, while the spectral distribution (line shapes) and line intensity ratios allow determining the plasma bulk temperature and the electron density via various methods (Stark broadening, dielectronic recombination, etc).
Consequently, XES is used in many fields of physics.
An important application of this technique is the inertial confinement fusion (ICF) science where a Deuterium-Tritium (DT) capsule is compressed in order to initiate fusion reactions and create a large amount of nuclear energy[4-7]. In this context, XES is set up to monitor X-rays generation and hot electrons (HE) impact on the target. These electrons have critical effects in fusion sciences due to their non-Maxwellian distribution. In indirect drive approach, HE may preheat the cold fuel thus inhibiting its desired compression[8]. In direct drive schemes, the role of HE can be positive or negative in dependence on conditions of HE generation (quantity, timing, and energy spectrum). In some approaches, e.g. in the shock ignition scheme, the moderate energy HE may deposit their energy in denser part of the plasma at surfaces of the fuel capsules, thus increasing their compression and improving the laser-target coupling. In this context, the mechanisms and parameters of the HE generation are intensively studied[9,10]. XES is also one of the most unique techniques to study matter irradiated by X-ray Free Electron Laser (XFEL). Here the high-resolution spectroscopy can be used to precisely characterize the kinetics of dense matter as well as atomic physics phenomena[11-14].

These applications demonstrate a need for precise diagnostics that are able to:
- Resolve and interpret the fine spectral features induced by HE,
- Investigate X-ray emission from highly transient environments such as those met in solid matter heating.

We report here on detailed studies of the $K\alpha_{1,2}$ lines emitted from hot and dense plasmas. These transitions are usually induced by HE and are present in the initial phase of the laser-matter interaction.
The interpretation of this emission is extremely demanding due to non-stationary environmental conditions and plasma kinetics. Even in experiments with ns lasers, the atomic physics involved in the HE induced emission from the start-up phase is strongly out-of-equilibrium. These conditions challenge atomic physics[3,15].
We will demonstrate the potential of high-resolution spectroscopy to describe the expansion of non-equilibrium plasmas during the first picoseconds of their lifetime. Within this period, the spatial extension of the plasma characterized by the bulk electron temperature 100-200 eV is estimated to approximately 100 µm above the original target surface[16], its lateral extent (typically at the level of 1 mm) depends on energy of HE produced. Particularly this region is of paramount interest in this study.
For this purpose, Cu M-shell charge states emission (with the valence electron in M-shell) is selected as these states only exist for bulk electron temperature lower than approximately 200 eV. This temperature is too low to ionize the inner-shell of mid-Z elements, and, consequently, X-ray lines are mostly induced by HE.

The article is organized as follows.
Section II presents the experimental details used to study the copper (Z = 29) plasma generated by the NANO2000 kJ-laser at the very beginning of the laser-plasma interaction.
Section III presents M-shell charge states Cu spectra and data analysis.
Section IV discusses the impact of the results for further studies.

2. Experiment

The NANO2000 Nd:Glass kJ-laser delivered a 750 J pulse in 1.5 ns at $\lambda = 1.054$ µm which was focused to a 15 µm diameter spot on 9-µm-thick Cu 99.5% foil, leading to a peak intensity I approximately equal to 2×10^{16} W.cm^{-2}.

The experimental scheme is shown on Figure 1.

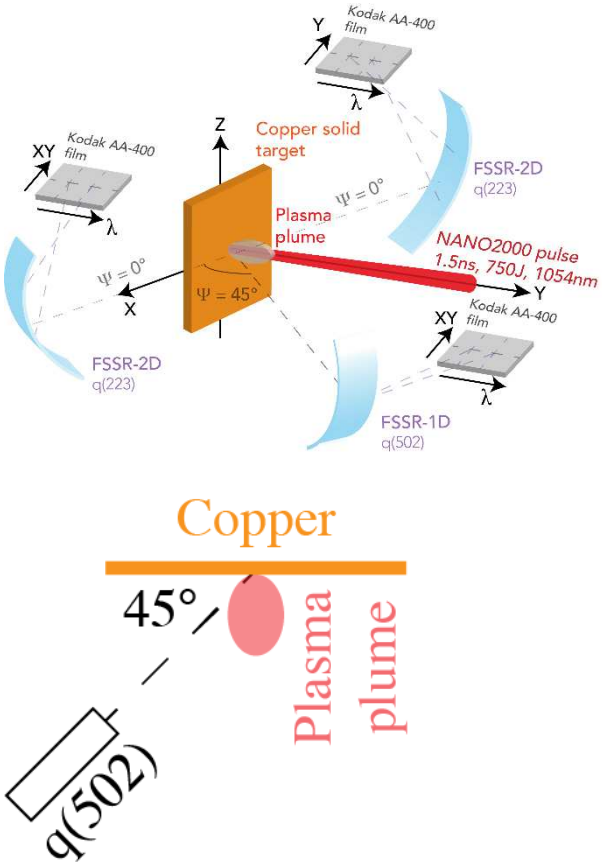

Figure 1: a. Scheme of the experimental setup includes two FSSR-2D spectrometers covering a large bandwidth from Kα to Lyα lines and one FSSR-1D with a narrow bandwidth centered on M-shell copper charge states. b. Scheme of the setup from the top showing the main diagnostic angle of view.

Three Johann spherical crystal spectrometers (FSSR) [3,17] were implemented in this experiment.
The two different configurations offer diverse combination of the spectral and spatial resolution.

In 1D configuration, the detector is placed on the Rowland circle and provides the best spectral resolution attainable. However, this geometry is constrained by the strictly defined crystal-detector distance and cannot always be applied due to geometrical restrictions of the target chamber.
In 2D configuration, the detector is placed outside the Rowland circle in the position fulfilling focal condition in the sagittal plane that is decisive for achieving the optimum spatial resolution. Consequently, this geometry is more convenient but if the source size is large (as in this experiment), the spectral resolution is reduced.

Dispersion planes of all crystals were placed parallel to the Z-axis.
Two FSSR-2D using quartz (223) crystals ($2d$ = 2.024 Å) were set up from both sides and tangentially to the target (Ψ = 0 ± 1°). These spectrometers provided spatial resolution along axis of the plasma plume expansion (Y).
The 2D spectrometers covered the wavelength bandwidth 1.39 < λ (Å) < 1.56. This allowed to record all X-ray lines within the spectral range from Cu Kα ($\lambda_{K\alpha1}$=1.5406 Å, $\lambda_{K\alpha2}$=1.5444 Å) to Lyα ($\lambda_{Ly\alpha3/2}$=1.4253 Å, $\lambda_{Ly\alpha1/2}$=1.4307 Å). This provides a survey of the plasma emission from a cold to heated target material with the bulk electron temperatures T_e at the level of 1-2 keV.

The quartz (502) crystal (2d = 1.624 Å) of the spectrometer used in FSSR-1D configuration provided the spatial resolution $\delta \approx$ 7 μm and the ray-traced spectral resolution $\lambda/\Delta\lambda \approx 3100$[18]. To achieve the maximum spatial resolution, the source-crystal SC = 178 mm and crystal-detector CD = 142 mm distances were chosen corresponding to a magnification of $M \approx 0.8$. The spectrometer observed the emission at the angle of $\Psi \approx 45°$ to the target and covered the wavelength range 1.526 < λ (Å) < 1.550.
The spatial resolution was provided in the XY plane, which allowed to record lines emitted along the target surface by low ionization Cu states[19].

To achieve the highest possible spatial and spectral resolution, Kodak AA-400 photographic film was used as detector. The spectra were scanned with an Epson V700 scanner providing a 4800 dpi (≈ 5.30 μm/px) resolution adequate to the film grain size.

3. Spectral analysis

3.1 Atomic physics processes

Hot electrons induced lines are commonly used to diagnose hot and dense plasmas.

The mechanisms of HE generation (e.g. parametric instabilities such as Stimulated Raman Scattering, Two-Plasmon Decay or Resonant Absorption) and transport in dense plasmas are reviewed in several recent papers[20-23].

For moderate intensities, the HE temperature can be roughly estimated as a function of the laser wavelength λ and the pulse intensity I_ω via the empirical Beg's scaling relation[24]:

$$T_{hot} \approx 215\left(\lambda^2[\mu m] I_\omega [10^{18}\ W.cm^{-2}]\right)^{\frac{1}{3}} keV \quad (3.1)$$

For a typical NANO2000 pulse, the hot electron temperature T_{hot} is approximately equal to 50 keV.
In comparison, a Cu K-shell electron has an ionization threshold in the range of energies 11.57 (Cu^{28+}) > E_i (keV) > 8.979 (Cu).
Hence, hot electrons can ionize the core inner-shells of Cu atoms as described by:

$$K^2L^8M^X + e^-_{hot} \rightarrow K^1L^8M^X + 2e^- \quad (3.2)$$

This unstable (autoionizing) atomic state leads to emission of Kα photons by filling the inner-shell vacancy:

$$K^1L^8M^XN^1 \rightarrow K^2L^7M^XN^1 + h\nu_{K\alpha} \quad (3.3)$$

The Kα radiation can be used to diagnose the plasma evolution from the start-up phase of the laser-matter interaction, as HE are usually generated also in the period of the rising laser pulse.

We note that the non-radiative Auger effect is minor for mid-Z elements as copper (cf. branching factor > 0.4)[15].

3.2 Spectral structure

The spectrum shown in Figure 2 was recorded with the FSSR-1D. The structure of the spectral profile emitted from the center of the focal spot is not governed by well-defined spectral peaks but by an overlap of X-ray lines emitted from different M-shell charge states. Because of the overlap of many line, the minimum effective spectral resolution determined by the width of the $K\alpha_2$ structure is $(\lambda/\Delta\lambda)_e \approx 1050$.
Due to the lateral HE propagation inside the cold material, which results in line emission from neutral to weakly ionized atoms, the extent of the $K\alpha_{1,2}$ emission is larger compared to the rest of the spectrum.

The M-shell is divided in three subshells (3s, 3p and 3d)[19].
The 3d-shell emission (corresponding to ions with valence electron in the 3d-subshell) is overlapped with the $K\alpha_1$ line of the Cu II (Cu^{1+}) charge state.
The 3p and 3s shell emission is emitted at shorter wavelengths. The overlap is weaker and several peaks can be well distinguished.

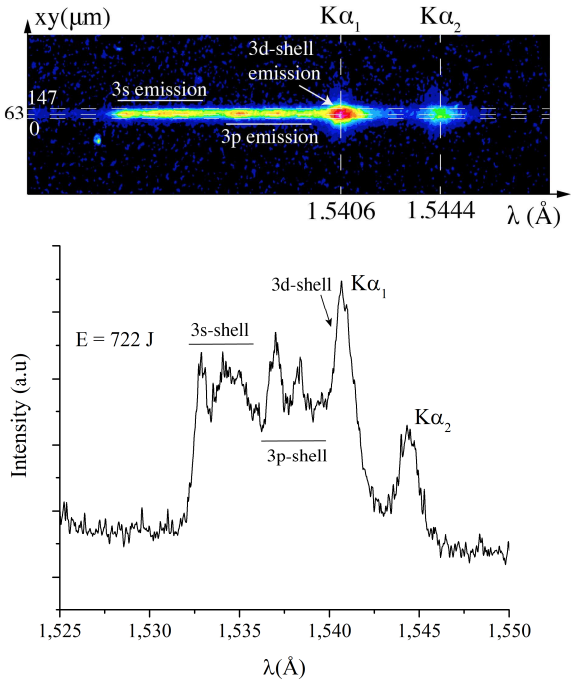

Figure 2: Spectrum recorded with the FSSR-1D and the reconstructed integrated profile. The emission of all M-shell charge states is divided in three sub-structures, 3d, 3p and 3s.

Figure 3 shows a survey spectrum obtained with one of the FSSR-2D. In addition to the clearly visible M-shell structure (marked by letter M in the Figure), the emission from all L-shell charge states is present. H-like emission was absent in spectral records because the maximum plasma temperature is too low to reach a sufficiently high population of this ionization state. The electron density is also too small to make such emission observable.
The survey spectra monitor the reproducibility of shots.

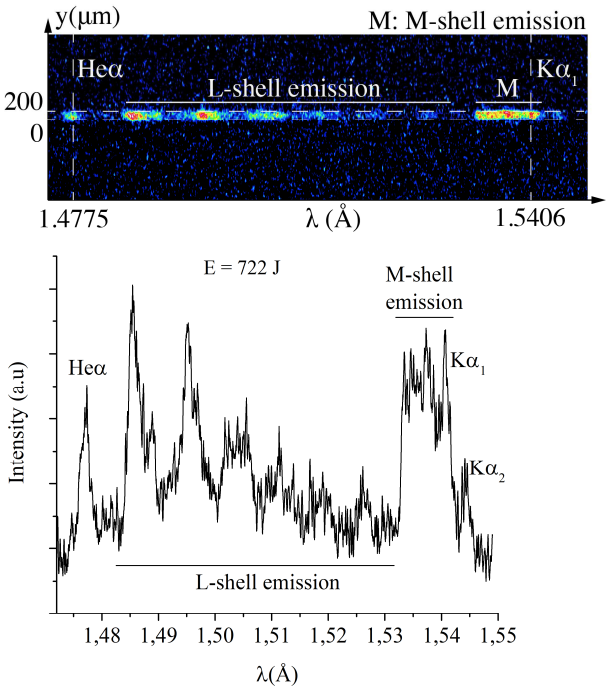

Figure 3: Spectral record of the FSSR-2D. The profile shows the emission of all M-shell and L-shell charge states.

Figure 4a presents the spatially resolved lineouts (in steps of 21 μm) from the spectrum taken with FSSR-1D.
Due to the angle of observation ($\Psi \approx 45°$), the area between -42 and 0 μm corresponds to the emission from the cold target. In the same time, the spectrum is spatially asymmetric with respect to the line of sight integration along different volumes of the plasma plume, (cf. Figure 1b).
Figure 4b shows a selected part (from 7 to 35 μm) of the spectrum resolved in steps of 7 μm. These lineouts demonstrate the capability of our diagnostic to describe the evolution of the M-shell structure. The area presented here is located at the edge between the cold and the hot material. At the position 0 μm (the same as the one on Figure 2), primarily Kα lines are visible above a weak emission from partially ionized atoms. At the position 42 μm, all the M-shell structure is well visible illustrating the temperature gradient.

Two dashed lines plotted in Figure 4 show the position of the cold $K\alpha_1$ ($\lambda = 1.5406$ Å) and $K\alpha_2$ lines ($\lambda = 1.5444$ Å). The spatially dependent red shift of these two lines reaches its maximum at the highest population of 3d-shell ionization states, which generate this shifted emission.
The application of a very high spatial and spectral resolution spectrometer is the only way to identify this phenomenon due to the very small energy variation of the 3d-shell Kα peaks.

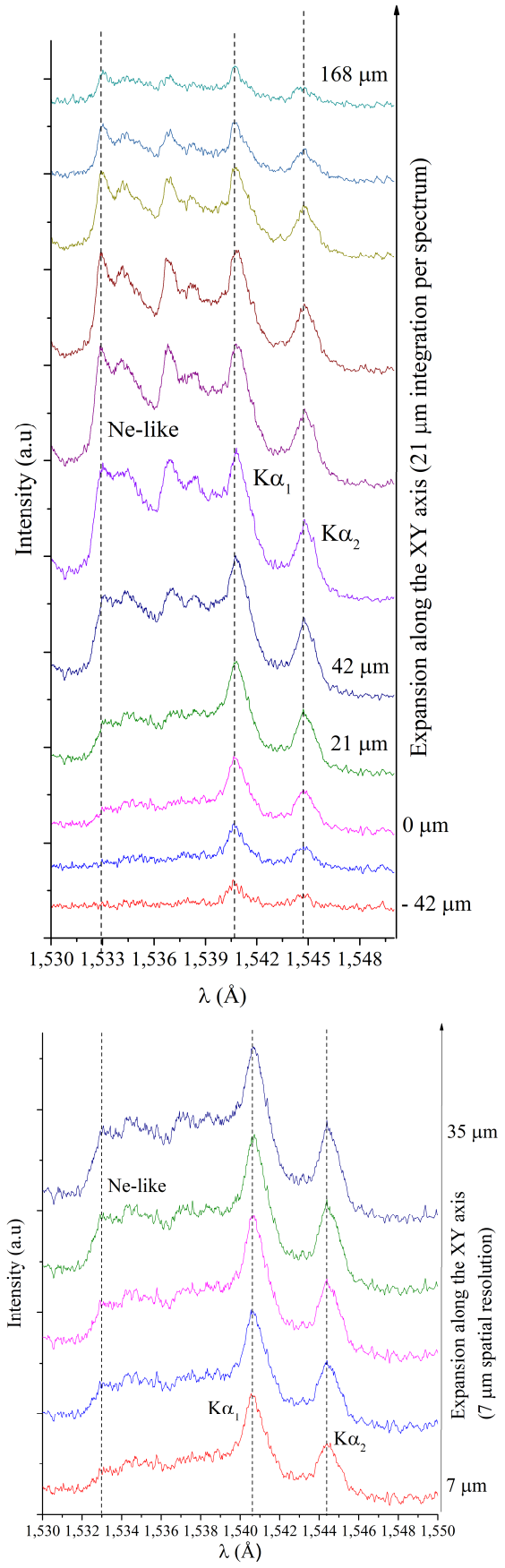

Figure 4: a. Spatially resolved spectrum recorded using FSSR-1D in steps of 21 µm. Between -42 and 0 µm (along the target), only the emission of 3d-shell states is visible. Emission from the plasma plume shows higher ionization states and variations in ionic fractions. Dashed lines represent the position of the cold Kα lines that shift to the red in the hot material.

b. Zoom of the emission from the plasma plume with the spatial resolution of a single detector pixel between 7 and 35μm from the focal spot centre.

This red shift, as well as the structures overlap, can be explained by the electronic screening effect. It causes the frequency shift of the emission from different charge states. However, inside the M-shell, this effect is very weak.
The screening effect calculated in Ref. 25 for a 2p-shell electron (involved in the Kα emission) interacting with another electron from the same sub-shell is $\sigma_{2p\_2p} = 0.3495$. It leads to a distinct separation between lines from different charge states as seen in Figure 3 in the L-shell emission area.
In contrast, for 3s and 3p-shell electrons, the screening constants are about an order of magnitude lower[25].

Figure 5 shows the wavelength shift of M-shell charge states Kα lines calculated with the Cowan's atomic structure code[26].

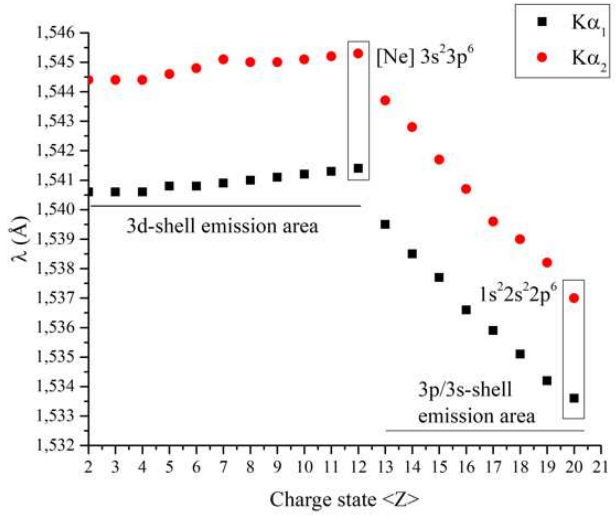

Figure 5: LSJ-split Hartree-Fock calculation of the M-shell charge states $K\alpha_1$ and $K\alpha_2$ lines wavelengths.

For 3d-shell charge states, a red shift occurs. It can be explained by the fact that FAC and Cowan includes configuration interaction (CI) and intermediate coupling (IC) together with angular momentum coupling (spin-orbit ect.) creating extremely complex structures. For example, with an open-3d shell configuration as the ones calculated here, the Kα line is a complex of more than 10 000 lines. Due to the very weak electronic screening of 3d-shell electrons, the effects of CI, IC and momentum coupling counterbalance it and creates the red shift.
Indeed, in the model[25] describing the screening between 2p electron and 3d electron predicts a value of $\sigma_{2p\_3d} = 0.0007$. This very low value becomes negligible due to the effects mentioned above.

We note that both Flexible Atomic Code and Cowan's atomic physics codes predict this behavior[26,27]. In addition, Doppler effect cannot cause the observed red shift. Due to our experimental configuration, the lines can only be unshifted (in optically thin plasmas observed parallel to the target surface) or blue-shifted due to the plasma expansion velocity component in the direction of spectra observation.
Also, only the 3d-shell structure is shifted whereas in contrast to the unshifted Ne-like emission.

Figure 6 represents an example of the plasma plume emission (integrated between distances of 42 and 63 μm). The solid pink curve is a fit calculated with the Cowan's atomic physics code coupled to a module of the MARIA code[28] using a Voigt profile adapted to the spectrometer spectral resolution. The other curves are the separated contributions from each subshell charge states.
Each ionization state is treated separately, and its corresponding intensity is fitted with a population factor f_k providing the spectral distribution.

$$I_\omega = \sum_k f_k \sum_{i,j} g_j^{(k)} A_{ji}^{(k)} \phi_{ji}^{(k)}(\omega, \omega_{ji}^{(k)}) \quad (3.4)$$

where index *(k)* indicates the considered ionization state (k = 0, 1, ..., 28). The index *j* corresponds to the upper state and *i* to the lower state level of the relevant transition,
g_j is the statistical weight, A_{ji} the radiative decay rate, ϕ_{ji} the line profile and ω_{ij} the line frequency.

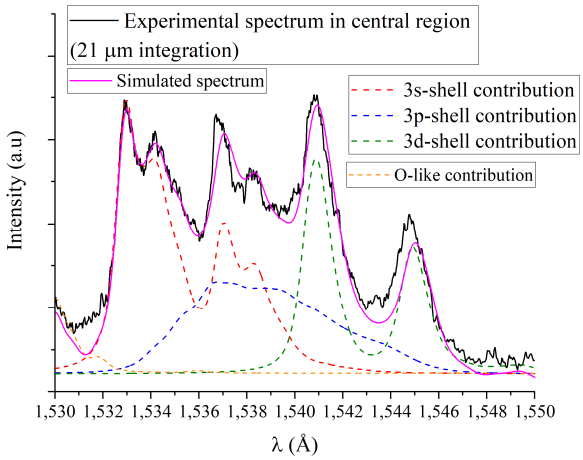

Figure 6: Spatially integrated spectrum observed in the central part of the plume between 42 and 63 µm. The pink curve shows the best fit. The other curves show the contribution from each subshell. The O-like contribution at the very left-hand part of the spectrum is also included.

The first lines emitted inside the plasma are induced by 3d-shell states, i.e. the low-ionization ones.
All 11 charges states of the 4s- and 3d-shell emit in a very narrow spectral range. Therefore, the intensity of this component is high and its shape is well defined.
The 3d-shell emission calculation includes three different configurations per charge state:

$$[Ar]3d^x4s^2$$

$$[Ar]3d^{x+1}4s^1$$

$$[Ar]3d^{x+2}$$

The 3d and 4s shells have very close and overlapping energy levels which is of paramount importance for precise calculation of Kα lines. Neglecting the 4s-shell in the calculation would lead to distorted results.
The 3p-shell ionization states generate a broad spectrum with low intensity compared to 3s- and 3d-shells.

Table 1 gives the fitted population factors f_k of 3p and 3s-subshells. These factors correspond to the intensity considered for each charge state distribution to obtain the best fit (the pink curve on Figure 6).

Error bars are determined by finding the limit for which the fit varies significantly. This operation is repeated for each charge state.

The determination of the 3d-subshell factors is possible but burdened with too high errors and are not included in this paper. Indeed, 10 different charge states emits almost at the same frequency making extremely approximate any fit.

Table 1: Fitted population factor f_k of different charge states from the 3p and 3s subshells.

Charge states	*Population factor f_k*
XX	$8.48\text{x}10^{-1} \pm 1.27\text{x}10^{-1}$
XIX	$4.32\text{x}10^{-2} \pm 1.30\text{x}10^{-2}$
XVIII	$1.08\text{x}10^{-2} \pm 1.08\text{x}10^{-3}$
XVII	$4.32\text{x}10^{-3} \pm 2.16\text{x}10^{-3}$
XVI	$4.63\text{x}10^{-3} \pm 2.32\text{x}10^{-3}$
XV	$4.63\text{x}10^{-4} \pm 4.63\text{x}10^{-5}$
XIV	$7.71\text{x}10^{-4} \pm 3.86\text{x}10^{-4}$
XIII	$7.71\text{x}10^{-5} \pm 1.54\text{x}10^{-5}$
XII	$9.25\text{x}10^{-4} \pm 1.39\text{x}10^{-4}$
XI	$7.71\text{x}10^{-5} \pm 2.31\text{x}10^{-5}$

The fit presents a very good correlation with experimental results. However, slight discrepancies can be observed mainly on the Kα$_2$ peak. Fitted population factors are averaged and do not reflect the charge states population at a precise point inside the plume due to time and line of sight integration. This explains these differences.

The population factor of the Cu XX charge states is much higher than the other ones in the table. The reason for this consists in the plasma kinetics as illustrated in Figure 7. This graph presents calculations from the FLYCHK code[29] for different bulk temperature conditions.

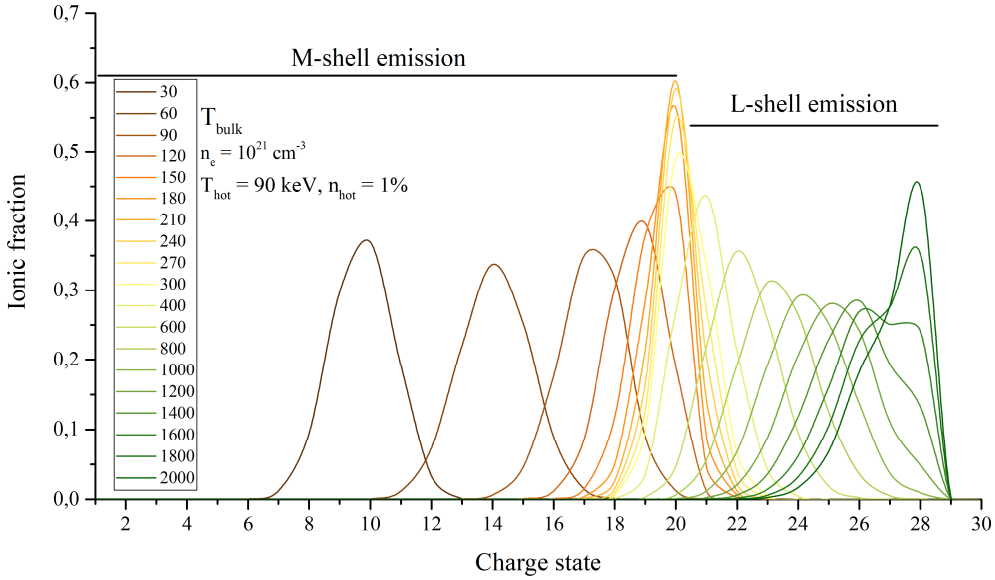

Figure 7: FLYCHK simulation of copper charge state distribution as a function of the plasma bulk temperature. The transition between M and L-shell can only be reached for high-temperature plasmas.

Charge state distribution evolves quickly within the temperature T_{bulk} = 0-100 eV, which shows that the temperature gradient along the line of sight is negligible for this application as 3d and 3p-shell charge states exist in the plasma for very low bulk temperatures only.
Between T_{bulk} = 100-200 eV, the distribution reaches a limit for Cu^{19+}. This state corresponds to the Ne-like (Cu XX) isoelectronic structure $1s^2\ 2s^2\ 2p^6$ and to the M-shell charge state limit. The Cu L-shell ionization threshold (E_{iL} = 1.697 keV) requires the high-temperature plasma to be crossed. It explains the saturation and the very high population factor for this charge state.

4. Conclusion

The highly resolved spectral emission from the plasma regions with strongly overlapping K-shell lines was analyzed by means of high-resolution X-ray spectroscopy based on application of spherically bent diffraction crystals.

The border area between the cold and the hot material was distinctly identified. The obtained spectra represent a high precision data set suitable for comparison of the experiment with the theory and hydro-simulations. This diagnostic gives a unique opportunity to study in detail X-ray lines induced by HE in transient environments.
Demonstrated analysis of 3p- and 3s-shell states emission, which resulted in determination of their population factors, represents a promising way to study the plasma temperature during its transient evolution. This is of primary importance for the initial phase of laser-solid interaction where the bulk electron temperature stays low.

The results presented here confirm previous theoretical predictions of the red Kα line shifts induced by the 3d-shell charge states. According to our knowledge, the high-precision experimental validation of these predictions has not been provided yet.
This counter-intuitive result may provide a new diagnostic tool for quantification of the HE generation and transport during the laser-matter interaction.

Acknowledgments

We thank the staff of the LULI2000 facility for their systematic help during the experiment.

This work has been done within the LABEX Plas@par project, and received financial state aid managed by the "Agence Nationale de la Recherche", as a part of the programme "Investissements d'Avenir" under the reference ANR-11-IDEX-0004-02.
The results were obtained within the state assignment of Ministry of Science and higher Education of Russia to JIHT RAS (topic #01201357846).
The work has been supported by the Competitiveness Program of NRNU MEPhI in the framework of the Russian Academic Excellence project.
The authors also acknowledge support from the Czech Republic Ministry of Education, Youth and Sports within targeted support of Large Infrastructures, ELI Beamlines Project LQ1606 of the National Program of Sustainability II and projects No. LM2015083 and LTT17015.

References

[1] H.R. Griem, Principles of Plasma Spectroscopy, Cambridge University Press, Cambridge, 1997. doi:10.1017/CBO9780511524578.
[2] F. B. Rosmej, V.A. Astapenko, V.A. Lisitsa, Plasma Atomic Physics, Springer, 2019. https://www.springer.com/us/book/9783030059668.
[3] O. Renner, F.B. Rosmej, Challenge of X-ray Spectroscopy in Investigations of Matter under Extreme Conditions, Matter Radiat. Extrem. 4 (2019).
[4] J. Lindl, Development of the indirect-drive approach to inertial confinement fusion and the target physics basis for ignition and gain, Phys. Plasmas. 2 (1995) 3933–4024. doi:10.1063/1.871025.
[5] S.H. Glenzer, B.J. MacGowan, P. Michel, N.B. Meezan, L.J. Suter, S.N. Dixit, J.L. Kline, G.A. Kyrala, D.K. Bradley, D.A. Callahan, E.L. Dewald, L. Divol, E. Dzenitis, M.J. Edwards, A. V. Hamza, C.A. Haynam, D.E. Hinkel, D.H. Kalantar, J.D. Kilkenny, O.L. Landen, J.D. Lindl, S. LePape, J.D. Moody, A. Nikroo, T. Parham, M.B. Schneider, R.P.J. Town, P. Wegner, K. Widmann, P. Whitman, B.K.F. Young, B. Van Wonterghem, L.J. Atherton, E.I. Moses, Symmetric Inertial Confinement Fusion Implosions at Ultra-High Laser Energies, Science (80-.). 327 (2010) 1228–1231. doi:10.1126/science.1185634.
[6] J.D. Lindl, P. Amendt, R.L. Berger, S.G. Glendinning, S.H. Glenzer, S.W. Haan, R.L. Kauffman, O.L. Landen, L.J. Suter, The physics basis for ignition using indirect-drive targets on the National Ignition Facility, Phys. Plasmas. 11 (2004) 339–491. doi:10.1063/1.1578638.
[7] S.Y. Gus'kov, Fast ignition of inertial confinement fusion targets, Plasma Phys. Reports. 39 (2013) 1–50. doi:10.1134/S1063780X13010017.
[8] S.P. Regan, N.B. Meezan, L.J. Suter, D.J. Strozzi, W.L. Kruer, D. Meeker, S.H. Glenzer, W. Seka, C. Stoeckl, V.Y. Glebov, T.C. Sangster, D.D. Meyerhofer, R.L. McCrory, E.A. Williams, O.S. Jones, D.A. Callahan, M.D. Rosen, O.L. Landen, C. Sorce, B.J. MacGowan, Suprathermal electrons generated by the two-plasmon-decay instability in gas-filled Hohlraums, Phys. Plasmas. (2010). doi:10.1063/1.3309481.
[9] R. Nora, W. Theobald, R. Betti, F.J. Marshall, D.T. Michel, W. Seka, B. Yaakobi, M. Lafon, C. Stoeckl, J. Delettrez, A.A. Solodov, A. Casner, C. Reverdin, X. Ribeyre, A. Vallet, J. Peebles, F.N. Beg, M.S. Wei, Gigabar spherical shock generation on the OMEGA laser, Phys. Rev. Lett. (2015). doi:10.1103/PhysRevLett.114.045001.
[10] E. Llor Aisa, X. Ribeyre, G. Duchateau, T. Nguyen-Bui, V.T. Tikhonchuk, A. Colaïtis, R. Betti, A. Bose, W. Theobald, The role of hot electrons in the dynamics of a laser-driven strong converging shock, Phys. Plasmas. (2017). doi:10.1063/1.5003814.
[11] S.M. Vinko, O. Ciricosta, B.I. Cho, K. Engelhorn, H.-K. Chung, C.R.D. Brown, T. Burian, J. Chalupský, R.W. Falcone, C. Graves, V. Hájková, A. Higginbotham, L. Juha, J. Krzywinski, H.J. Lee, M. Messerschmidt, C.D. Murphy, Y. Ping, A. Scherz, W. Schlotter, S. Toleikis, J.J. Turner, L. Vysin, T. Wang, B. Wu, U. Zastrau, D. Zhu, R.W. Lee, P.A. Heimann, B. Nagler, J.S. Wark, Creation and diagnosis of a solid-density plasma with an X-ray free-electron laser, Nature. 482 (2012) 59–62. doi:10.1038/nature10746.
[12] O. Ciricosta, S.M. Vinko, H.-K. Chung, B.-I. Cho, C.R.D. Brown, T. Burian, J. Chalupský, K. Engelhorn, R.W. Falcone, C. Graves, V. Hájková, A. Higginbotham, L. Juha, J. Krzywinski, H.J. Lee, M. Messerschmidt, C.D. Murphy, Y. Ping, D.S. Rackstraw, A. Scherz, W. Schlotter, S. Toleikis, J.J. Turner, L. Vysin, T. Wang, B. Wu, U. Zastrau, D. Zhu, R.W. Lee, P. Heimann, B. Nagler, J.S. Wark, Direct Measurements of the Ionization Potential Depression in a Dense Plasma, Phys. Rev. Lett. 109 (2012) 065002. doi:10.1103/PhysRevLett.109.065002.
[13] F.B. Rosmej, A. Moinard, O. Renner, E. Galtier, J.J. Lee, B. Nagler, P.A. Heimann, W. Schlotter, J.J. Turner, R.W. Lee, M. Makita, D. Riley, J. Seely, XFEL resonant photo-pumping of dense plasmas and dynamic evolution of autoionizing core hole states, J. Phys. Conf. Ser. 688 (2016) 012093. doi:10.1088/1742-6596/688/1/012093.
[14] E. Galtier, F.B. Rosmej, T. Dzelzainis, D. Riley, F.Y. Khattak, P. Heimann, R.W. Lee, A.J. Nelson, S.M. Vinko, T. Whitcher, J.S. Wark, T. Tschentscher, S. Toleikis, R.R. Fäustlin, R. Sobierajski, M. Jurek, L. Juha, J. Chalupsky, V. Hajkova, M. Kozlova, J. Krzywinski, B. Nagler, Decay of Cystalline Order and Equilibration during the Solid-to-Plasma Transition Induced by 20-fs Microfocused 92-eV Free-Electron-Laser Pulses, Phys. Rev. Lett. 106 (2011) 164801. doi:10.1103/PhysRevLett.106.164801.
[15] F. B. Rosmej, Handbook for Highly Charged Ion Spectroscopic Research, CRC Press, 2012.
[16] M. Smid et al., Nature Comm, Submitted (2019)
[17] A.Y. Faenov, S.A. Pikuz, A.I. Erko, B.A. Bryunetkin, V.M. Dyakin, G. V Ivanenkov, A.R. Mingaleev, T.A. Pikuz, V.M. Romanova, T.A. Shelkovenko, High-performance x-ray spectroscopic devices for plasma microsources investigations, Phys. Scr. 50 (1994) 333–338. doi:10.1088/0031-8949/50/4/003.
[18] S.G. Podorov, O. Renner, O. Wehrhan, E. Förster, Optimized polychromatic x-ray imaging with asymmetrically cut bent crystals, J. Phys. D. Appl. Phys. 34 (2001) 2363–2368. doi:10.1088/0022-3727/34/15/317.

[19] F.P. Condamine, M. Šmíd, O. Renner, M. Dozières, F. Thais, P. Angelo, F.B. Rosmej, M-shell resolved high-resolution X-ray spectroscopic study of transient matter evolution driven by hot electrons in kJ-laser produced plasmas, in: 2017: p. 060001. doi:10.1063/1.4975725.

[20] W. Theobald, A. Bose, R. Yan, R. Betti, M. Lafon, D. Mangino, A.R. Christopherson, C. Stoeckl, W. Seka, W. Shang, D.T. Michel, C. Ren, R.C. Nora, A. Casner, J. Peebles, F.N. Beg, X. Ribeyre, E. Llor Aisa, A. Colaïtis, V. Tikhonchuk, M.S. Wei, Enhanced hot-electron production and strong-shock generation in hydrogen-rich ablators for shock ignition, Phys. Plasmas. 24 (2017) 120702. doi:10.1063/1.4986797.

[21] D. Batani, L. Antonelli, F. Barbato, G. Boutoux, A. Colaïtis, J.-L. Feugeas, G. Folpini, D. Mancelli, P. Nicolai, J. Santos, J. Trela, V. Tikhonchuk, J. Badziak, T. Chodukowski, K. Jakubowska, Z. Kalinowska, T. Pisarczyk, M. Rosinski, M. Sawicka, F. Baffigi, G. Cristoforetti, F. D'Amato, P. Koester, L.A. Gizzi, S. Viciani, S. Atzeni, A. Schiavi, M. Skoric, S. Gus'kov, J. Honrubia, J. Limpouch, O. Klimo, J. Skala, Y.J. Gu, E. Krousky, O. Renner, M. Smid, S. Weber, R. Dudzak, M. Krus, J. Ullschmied, Progress in understanding the role of hot electrons for the shock ignition approach to inertial confinement fusion, Nucl. Fusion. 59 (2019) 032012. doi:10.1088/1741-4326/aaf0ed.

[22] O. Renner, M. Šmíd, D. Batani, L. Antonelli, Suprathermal electron production in laser-irradiated Cu targets characterized by combined methods of x-ray imaging and spectroscopy, Plasma Phys. Control. Fusion. 58 (2016) 075007. doi:10.1088/0741-3335/58/7/075007.

[23] A. Colaïtis, G. Duchateau, X. Ribeyre, Y. Maheut, G. Boutoux, L. Antonelli, P. Nicolaï, D. Batani, V. Tikhonchuk, Coupled hydrodynamic model for laser-plasma interaction and hot electron generation, Phys. Rev. E. 92 (2015) 041101. doi:10.1103/PhysRevE.92.041101.

[24] F.N. Beg, A.R. Bell, A.E. Dangor, C.N. Danson, A.P. Fews, M.E. Glinsky, B.A. Hammel, P. Lee, P.A. Norreys, M. Tatarakis, A study of picosecond laser–solid interactions up to 10 19 W cm −2, Phys. Plasmas. 4 (1997) 447–457. doi:10.1063/1.872103.

[25] G. Faussurier, C. Blancard, A. Decoster, New screening coefficients for the hydrogenic ion model including l-splitting for fast calculations of atomic structure in plasmas, J. Quant. Spectrosc. Radiat. Transf. 58 (1997) 233–260. doi:10.1016/S0022-4073(97)00018-6.

[26] R.D. Cowan, The Theory of Atomic Structure and Spectra, University of California Press, Berkeley, 1981.

[27] M.F. Gu, The flexible atomic code, Can. J. Phys. 86 (2008) 675–689. doi:10.1139/p07-197.

[28] F.B. Rosmej, Hot electron x-ray diagnostics, J. Phys. B At. Mol. Opt. Phys. 30 (1997) L819–L828. doi:10.1088/0953-4075/30/22/007.

[29] H.-K. Chung, M.H. Chen, W.L. Morgan, Y. Ralchenko, R.W. Lee, FLYCHK: Generalized population kinetics and spectral model for rapid spectroscopic analysis for all elements, High Energy Density Phys. 1 (2005) 3–12. doi:10.1016/j.hedp.2005.07.001.